

1

## 2 **Supplementary Information for**

### 3 **Neuromechanical wave resonance in jellyfish swimming**

4 **A P Hoover, N W Xu, B J Gemmell, S P Colin, J H Costello, J O Dabiri, and L A Miller**

5 **Alexander P Hoover.**  
6 **E-mail: ahoover1@uakron.edu**

#### 7 **This PDF file includes:**

8 Figs. S1 to S2  
9 Table S1  
10 Legends for Movies S1 to S8  
11 SI References

#### 12 **Other supplementary materials for this manuscript include the following:**

13 Movies S1 to S8

14 **Materials.** The materials used to calculate the experimental muscle wave speeds included *Aurelia aurita* medusa ( $N = 5$ , 8.2 to  
 15 11.1 cm in bell diameter, obtained from Cabrillo Marine Aquarium in San Pedro, CA, USA); a wire electrode connected to a  
 16 MyoPacer Cell Stimulator (IonOptix, Westwood, MA, USA); visible implant elastomer tags (Northwest Marine Technology,  
 17 Shaw Island, WA, USA); and a Cyber-shot DSC-RX100 Digital Camera (Sony Corporation of America, New York City, NY,  
 18 USA). Wire electrodes comprised perfluoroalkoxy-coated silver wire (bare diameter of  $76.2 \mu\text{m}$ , coated diameter of  $139.7 \mu\text{m}$ )  
 19 and platinum rod tips (diameter of  $254.0 \mu\text{m}$ ) from A-M Systems (Sequim, WA, USA), connected in series to TinyLily 10402  
 20 light-emitting diodes (TinyCircuits, Akron, OH, USA).

## 21 **Methods.**

22 **Fluid-structure interaction.** Fluid-structure interaction systems are ubiquitous throughout the biological world, with many  
 23 examples in locomotion ranging from insects flying to fish undulating (1–4). A number of computational approaches have been  
 24 developed to examine these systems (5, 6). The immersed boundary (IB) method (7) is one such approach to numerically  
 25 solving fully-coupled fluid-structure interaction problems. First introduced by Peskin in the 1970s to study cardiovascular  
 26 dynamics of the heart (8), the IB method has since been applied to many fluid-structure interaction problems in biology in the  
 27 low to intermediate Reynolds number regime (9–22).

28 The IB formulation of the fluid-structure interaction system employs an Eulerian description of the equations of fluid motion  
 29 and a Lagrangian description for the immersed structure. Let  $\mathbf{x} = (x, y, z) \in \Omega$  denote physical Cartesian coordinates, with  
 30  $\Omega$  denoting the physical region occupied by the fluid-structure system. Let  $\mathbf{X} = (X, Y, Z) \in U$  denote Lagrangian material  
 31 coordinates that describe the immersed structure, with  $U$  denoting the Lagrangian coordinate domain. The physical position of  
 32 material point  $\mathbf{X}$  at time  $t$  is mapped by  $\chi(\mathbf{X}, t) \in \Omega$ . The physical region occupied by the structure at time  $t$  is  $\chi(U, t) \subset \Omega$ .

33 The immersed boundary formulation of the equations of motion is given by

$$34 \quad \rho \left( \frac{\partial \mathbf{u}(\mathbf{x}, t)}{\partial t} + \mathbf{u}(\mathbf{x}, t) \cdot \nabla \mathbf{u}(\mathbf{x}, t) \right) = -\nabla p(\mathbf{x}, t) + \mu \nabla^2 \mathbf{u}(\mathbf{x}, t) + \mathbf{f}(\mathbf{x}, t) \quad [1]$$

$$35 \quad \nabla \cdot \mathbf{u}(\mathbf{x}, t) = 0 \quad [2]$$

$$36 \quad \mathbf{f}(\mathbf{x}, t) = \int_U \mathbf{F}(\mathbf{X}, t) \delta(\mathbf{x} - \chi(\mathbf{X}, t)) d\mathbf{X} \quad [3]$$

$$37 \quad \int_U \mathbf{F}(\mathbf{X}, t) \cdot \mathbf{V}(\mathbf{X}) d\mathbf{X} = - \int_U \mathbb{P}(\mathbf{X}, t) : \nabla_{\mathbf{x}} \mathbf{V}(\mathbf{X}) d\mathbf{X} \quad [4]$$

$$38 \quad \frac{\partial \chi(\mathbf{X}, t)}{\partial t} = \int_{\Omega} \mathbf{u}(\mathbf{x}, t) \delta(\mathbf{x} - \chi(\mathbf{X}, t)) d\mathbf{x} \quad [5]$$

39 in which  $\rho$  is the fluid density,  $\mu$  is the dynamic viscosity,  $\mathbf{u}(\mathbf{x}, t) = (u_x, u_y, u_z)$  is the Eulerian material velocity field, and  
 40  $p(\mathbf{x}, t)$  is the Eulerian pressure field. Here,  $\mathbf{f}(\mathbf{x}, t)$  and  $\mathbf{F}(\mathbf{X}, t)$  are equivalent Eulerian and Lagrangian force densities.  $\mathbf{F}$   
 41 is defined in terms of the first Piola-Kirchhoff solid stress in Eq. 4 using a weak formulation, in which  $\mathbf{V}(\mathbf{X})$  is an arbitrary  
 42 Lagrangian test function. The Dirac delta function  $\delta(\mathbf{x})$  appears as the kernel of the integral transforms, Eqs. 3 and 5, that  
 43 connect the Eulerian and Lagrangian frames.

44 For this study, a hybrid finite difference/finite element version of the immersed boundary method (IB/FE) is used to  
 45 approximate Eqs. 1-5. The IB/FE method uses a finite difference formulation for the Eulerian equations and a finite element  
 46 formulation to describe the solid body. More details on the IB/FE method can be found in (23, 24).

47 **Bell model and geometry.** In this section we describe the structural model of the bell, which was previously developed in  
 48 (18, 20). The computational bell's motion is a result of the interaction between the passive elastic material properties of the  
 49 bell, the active tension model, and the local fluid environment. Note that none of the motion is prescribed. The structural  
 50 stresses are calculated using the first Piola-Kirchhoff stress tensor

$$51 \quad \mathbb{P} = \mathbb{P}_p + \mathbb{P}_a, \quad [6]$$

52 in which  $\mathbb{P}_p$  describes the passive elasticity of the body and  $\mathbb{P}_a$  describes the active tension generated by the muscle model.

53 The bell's mesoglea has passive elastic properties that are described using a neo-Hookean material model

$$54 \quad \mathbb{P}_p = \nu(\mathbb{F} - \mathbb{F}^{-T}) \quad [7]$$

55 in which  $\mathbb{F} = \frac{\partial \mathbf{x}}{\partial \mathbf{X}}$  is the deformation gradient and  $\nu$  is the elastic modulus of the material. For this model,  $\nu$  is held fixed  
 56 throughout the bell. Motivation for the geometry of the bell and its elastic properties can be found in (18, 20).

57 The muscle activation wave is modeled with a time-dependent active stress on the bell. This circumferentially-oriented  
 58 stress is applied over the lower portion of the bell margin where the coronal swimming musculature is present. The active  
 59 stress is calculated via

$$60 \quad \mathbb{P}_a = JT\mathbb{F}\mathbf{f}_0\mathbf{f}_0^T \quad [8]$$

61 in which  $J = \det(\mathbb{F})$  is the Jacobian of  $\mathbb{F}$ ,  $T$  is the magnitude of the prescribed tension, and  $\mathbf{f}_0$  is the fiber direction vector  
 62 of the prescribed tension with respect to the reference configuration. Here  $\mathbf{f}_0$  is follows from the coronal orientation of the

**Table S1. Table of dimensional parameters for the bell's structural model. In this study the elastic modulus,  $\nu$ , and the maximum tension,  $T_{\max}$ , are varied in proportion to one another and the values reported here are for the reference configuration.**

Parameter	Symbol	Value
Elastic modulus	$\nu_{\text{ref}}$	100.0 Pa
Horizontal axis (exumbrellar)	$a_{\text{ex}}$	0.02 m
Horizontal axis (subumbrellar)	$a_{\text{sub}}$	0.019 m
Vertical axis (exumbrellar)	$b_{\text{ex}}$	0.016 m
Vertical axis (subumbrellar)	$b_{\text{sub}}$	0.01 m
Maximum tension	$T_{\max}^{\text{ref}}$	100.0 N
Activation inflection point	$Z_{\text{lim}}$	0.0075 m
Musculature variable (spatial)	$\sigma_s$	2000.0 m <sup>-1</sup>
Musculature variable (temporal)	$\sigma_t$	200.0 s <sup>-1</sup>
Offset	$t_0$	0.1 s
Activation wave cycle period	$\gamma$	0.3 sec

subumbrellar swimming musculature in the undeformed configuration. In this study,  $T_{max}$  is held in proportion to  $\nu$ . Further details and motivation for this muscle model may be found in (18, 20).

The three-dimensional bell model geometry is chosen to be similar to that of an oblate rowing jellyfish, such as the moon jellyfish *Aurelia* spp. The bell shape was parametrized using a hemiellipsoid description for the exumbrellar (ex) and subumbrellar (sub) surfaces via

$$\frac{(X - X_c)^2 + (Y - Y_c)^2}{a_{ex,sub}^2} + \frac{(Z - Z_c)^2}{b_{ex,sub}^2} = 1 \text{ for } Z \geq 0, \quad [9]$$

in which  $\mathbf{X}_c = (X_c, Y_c, Z_c)$  is the center of the ellipsoid,  $a_{ex,sub}$  is the radial axis of the subumbrellar and exumbrellar surfaces of the bell, respectively, and  $b_{ex,sub}$  is its vertical axis (see Table S1 and Fig. S1). Variation in the bell thickness due to differences in the exumbrellar and subumbrellar dimensions accounts for variation in the elastic profile of the bell, where the thinner bell margin is more flexible than the thicker center of the bell.

Below we describe how the activation wave is applied to the bell. The tension,  $T$ , applied at point  $\mathbf{X}$ , varies in time and with respect to the height of the bell in its reference configuration,  $Z$ , and is given by

$$T = T_{max}\alpha(\theta, t)\beta(Z) \quad [10]$$

in which  $T_{max}$  is the maximum applied tension,  $\alpha(\theta, t)$  is a temporal-spatial parametrization of the activation and release of muscular tension with respect to the angular coordinate of the margin ( $\theta = \cos^{-1}(X/\sqrt{X^2 + Y^2})$ ), and  $\beta(Z)$  is a spatial parametrization of the distribution of the subumbrellar musculature. We remark that  $0 \leq \alpha(\theta, t), \beta(Z) \leq 1$ . A value of 0 implies either that no muscle is present or that the muscle is not activated.

Because the subumbrellar musculature does not extend throughout the bell, tension is applied at the margin of the bell. The region of activation is parameterized via

$$\beta(Z) = 1.0 - \frac{1}{1 + \exp(-\sigma_s(Z - Z_{lim}))} \quad [11]$$

in which  $\theta_s$  characterizes the transition from an area of active tension to an area where no tension is applied, and  $Z_{lim}$  is the inflection point of the transition (see Fig. S1).

In this study, two sets of simulations are performed using different temporal patterns of activation described by  $\alpha(\theta, t)$ . The first set of simulations are performed to measure the material wave speed of the computational bell immersed in the viscous fluid. Active tension is applied uniformly to a quarter of the bell

$$\alpha(\theta, t) = \begin{cases} 1 & \text{for } \theta < \pi/8 \\ 0 & \text{for } \theta \geq \pi/8 \end{cases}. \quad [12]$$

The resulting deformation causes a deflection in the bell margin that is propagated along the rim of the bell. The time it takes for the deflection to arrive to the opposite side of the bell, after the onset of the active tension, is then used to calculate the model's material wave speed,  $c_r$ . This is done for bells with elastic moduli of  $1/4\nu_{ref}$ ,  $\nu_{ref}$ , and  $4\nu_{ref}$ . Note that these numerical experiments are performed as it is not straightforward to calculate the wave speed analytically as the effective mass of the bell is difficult to determine for unsteady pulsing at these Reynolds numbers. The resulting bell deformations for this study are shown in Supplementary Videos 1 and 2.

The second set of simulations are used to quantify the turning performance as a function of both the bell's elastic profile and the neural dynamics of traveling activation waves generated by a single pacemaker. In these simulations, a wave of tension is applied and released to induce an asymmetrical contraction of the bell's. Here  $\alpha(\theta, t)$  is parametrized

$$\alpha(\theta, t) = \frac{1}{1 + \exp(-\sigma_t\pi t^*)} - \frac{1}{1 + \exp(-\sigma_t\pi(t^* - t_{dur}/\gamma))} \quad [13]$$

$$t^* = (t - \theta\tau/\pi)/\gamma - \lfloor (t - \theta\tau/\pi)/\gamma \rfloor - t_0/\pi \quad [14]$$

in which  $\gamma$  is the period of an activation wave cycle,  $t_0$  is an offset time for the initial function,  $\sigma_t$  characterizes the speed of muscular activation and release,  $t_{dur}$  describes the duration of contraction, and  $\tau$  represents the passage time it takes for a wave to travel from one side of the bell to the other. The resulting kinematics for a reference case ( $\nu = \nu_{ref}, \tau = 10^{-1}$ ) are shown in Supplementary Videos 3 and 4, as well as Supplementary Videos 5 and 6, which also show the velocity vectors and vorticity.

For the second set of simulations, each simulation was assigned a passage time,  $\tau = 10^\rho$ , for the activation wave to travel from one side of the bell to the opposite side. The range of passage times used were chosen by setting  $\rho = -2.0$  to  $0.0$  in  $0.2$  increments. Note that the activation wave speed corresponds to the passage time,  $c_a = r\pi\tau$ , where  $r$  ( $= 0.02$  m) is the radius of the bell. The resulting kinematics for comparing the effects of activation wave speed and bell stiffness are shown in Supplementary Videos 7 and 8.

**A. Circulation analysis.** To quantify how the fluid is affected by the activation wave speed, an analysis of the circulation of the stopping vortex ring. Following the methods of (25) and used by the authors previously in (18, 20), the circulation,  $\Gamma$ , is calculated as the integral of vorticity over the area of the vortex ring along the central plane as

$$\Gamma = \int \omega_y(x, 0, z, t) dx dz. \quad [15]$$

Due to the radial symmetry of the stopping vortex ring, the circulation was measured on the inside and outside of the turn.

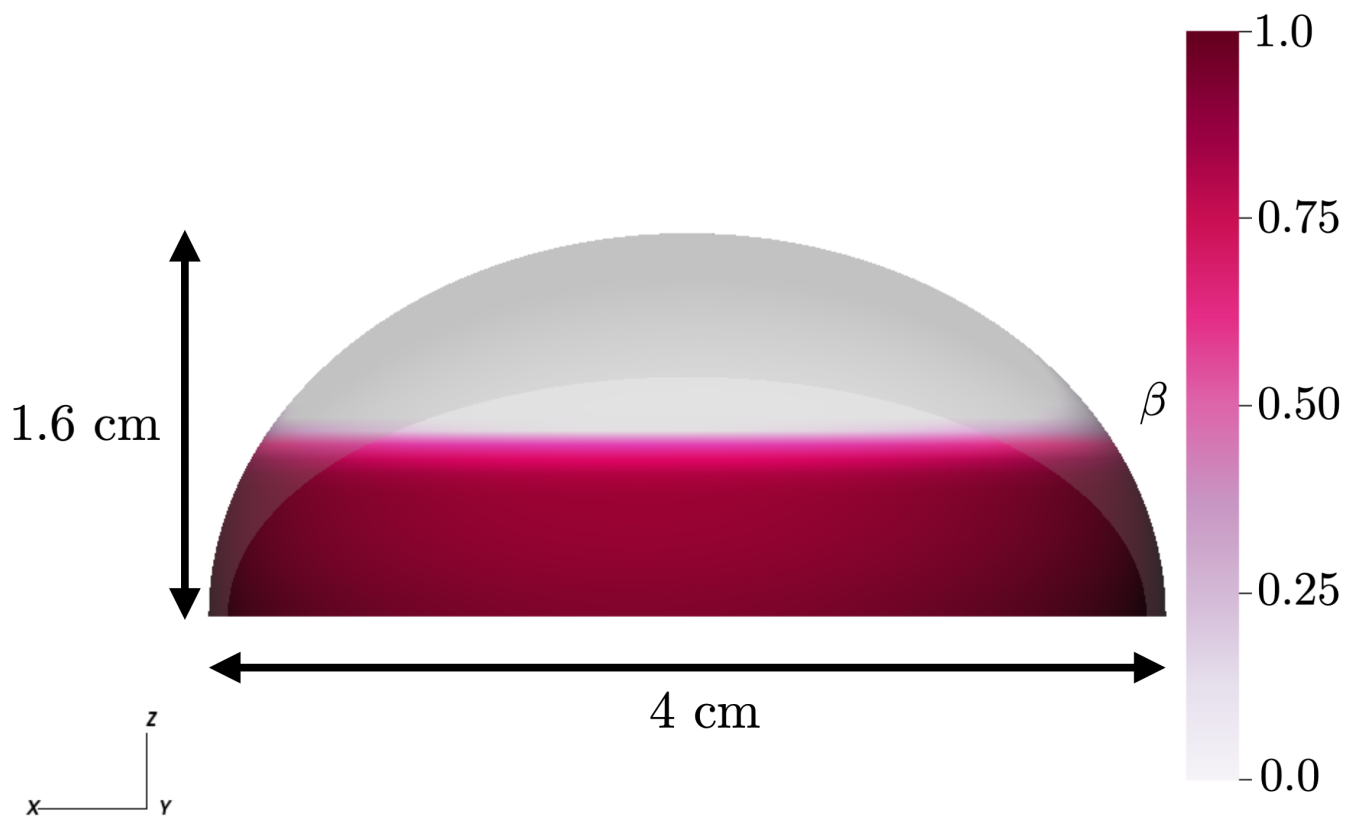


**Fig. S1.** A diagram of the bell model geometry with the bell color corresponding to the spatial musculature parametrization,  $\beta = \beta(Z)$ . Here  $\beta = 1$  corresponds to region where tension is applied during an activation wave, and  $\beta = 0$  corresponds to region where muscular activation is absent.

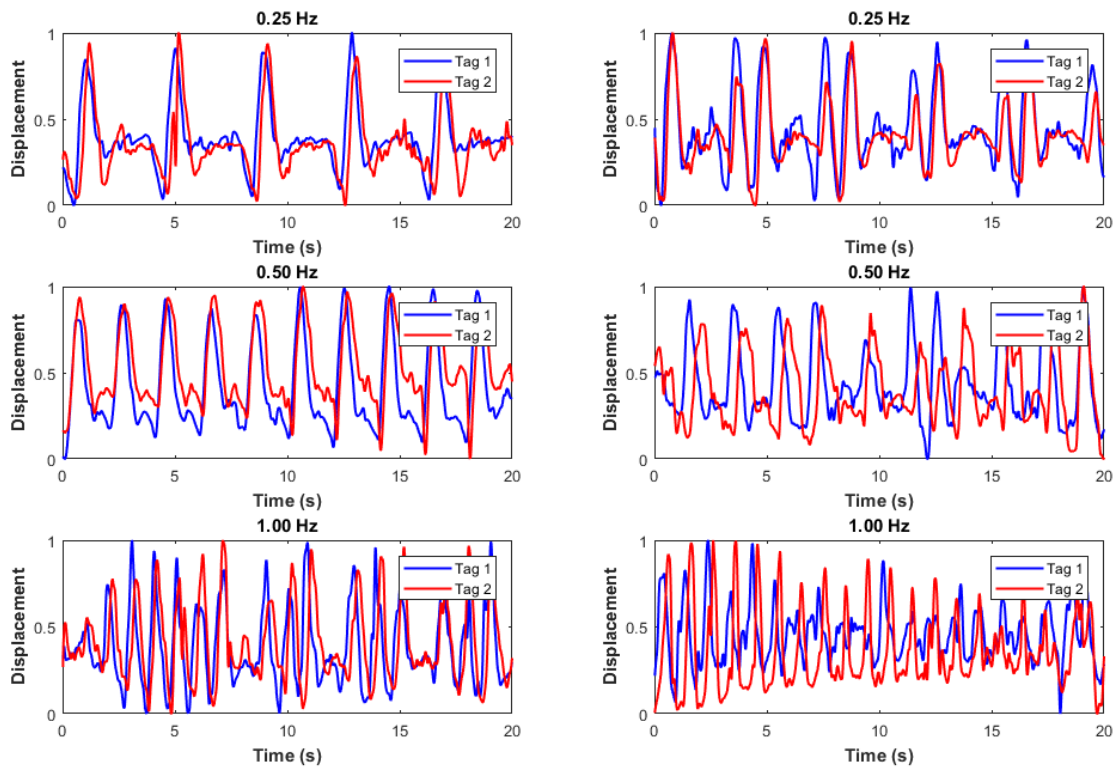


**Fig. S2.** Tag displacements (normalized from 0 to 1) for two particle tags injected into each animal ( $N = 6$  cases, using  $N = 5$  animals, driven at 0.25, 0.50, and 1.00 Hz). The time delays between tags 1 and 2 were used to obtain muscle wave propagation speeds.

115 **Movie S1.** The resulting kinematics for three model bells using  $\nu = 1/4\nu_{ref}$  (left),  $\nu_{ref}$  (middle), and  $4\nu_{ref}$   
116 (right) during the material wave speed study.

117 **Movie S2.** The radial displacement of the bell margin using  $\nu = \nu_{ref}$  during the material wave speed study.  
118 The region where tension is applied is highlighted in pink. The colormap shows radial displacement from the  
119 resting configuration. The speed of the displacement wave is the material wave speed.

120 **Movie S3.** The resulting kinematics of the bell ( $\nu = \nu_{ref}, c_a = r\pi 10^{-0.6}$ ) during the activation wave study. Note  
121 the symmetry of the bell across the vertical plane. The rim of the bell margin is in red to visualize the  
122 motion.

123 **Movie S4.** The resulting kinematics of the bell ( $\nu = \nu_{ref}, c_a = r\pi 10^{-0.6}$ ) during the activation wave study. The  
124 region where applied tension is present is highlighted in pink.

125 **Movie S5.** Cut out of the half-plane of the bell ( $\nu = \nu_{ref}, c_a = r\pi 10^{-0.6}$ ) during the activation wave study, with  
126 out-of-plane vorticity and velocity vectors plotted on the center plane.

127 **Movie S6.** Cut out of the half-plane of the bell ( $\nu = \nu_{ref}, c_a = r\pi 10^{-0.6}$ ) during the activation wave study, with  
128 isocontours of vorticity magnitude plotted on the half-plane.

129 **Movie S7.** The resulting kinematics of the three bell with a fixed elastic modulus ( $\nu = \nu_{ref}$ ) for three different  
130 waves speeds:  $c_a = r\pi 10^0$  (left);  $c_a = r\pi 10^{-1}$  (middle);  $c_a = r\pi 10^{-1}$  (right). The region where applied tension is  
131 present is highlighted in pink.

132 **Movie S8.** The resulting kinematics of the three bell with a fixed wave speed ( $c_a = r\pi 10^{-1}$ ) for three different  
133 elastic moduli:  $\nu = 1/4\nu_{ref}$  (left);  $\nu = \nu_{ref}$  (middle);  $\nu = 4\nu_{ref}$  (right). The region where applied tension is  
134 present is highlighted in pink

## 135 References

- 136 1. ED Tytell, CY Hsu, LJ Fauci, The role of mechanical resonance in the neural control of swimming in fishes. *Zoology* **117**,  
137 48–56 (2014).
- 138 2. AJ Bergou, L Ristroph, J Guckenheimer, I Cohen, ZJ Wang, Fruit flies modulate passive wing pitching to generate in-flight  
139 turns. *Phys. review letters* **104**, 148101 (2010).
- 140 3. L Ristroph, et al., Dynamics, control, and stabilization of turning flight in fruit flies in *Natural locomotion in fluids and on*  
141 *surfaces*. (Springer), pp. 83–99 (2012).
- 142 4. APS Bhalla, R Bale, BE Griffith, NA Patankar, A unified mathematical framework and an adaptive numerical method for  
143 fluid–structure interaction with rigid, deforming, and elastic bodies. *J. Comput. Phys.* **250**, 446–476 (2013).
- 144 5. R Mittal, G Iaccarino, Immersed boundary methods. *Annu. Rev. Fluid Mech.* **37**, 239–261 (2005).
- 145 6. BE Griffith, NA Patankar, Immersed methods for fluid–structure interaction. *Annu. Rev. Fluid Mech.* **52**, 421–448 (2020).
- 146 7. CS Peskin, The immersed boundary method. *Acta numerica* **11**, 479–517 (2002).
- 147 8. CS Peskin, Numerical analysis of blood flow in the heart. *J. computational physics* **25**, 220–252 (1977).
- 148 9. LJ Fauci, CS Peskin, A computational model of aquatic animal locomotion. *J. Comput. Phys.* **77**, 85–108 (1988).
- 149 10. ED Tytell, CY Hsu, TL Williams, AH Cohen, LJ Fauci, Interactions between internal forces, body stiffness, and fluid  
150 environment in a neuromechanical model of lamprey swimming. *Proc. Natl. Acad. Sci.* **107**, 19832–19837 (2010).
- 151 11. LA Miller, CS Peskin, When vortices stick: an aerodynamic transition in tiny insect flight. *J. Exp. Biol.* **207**, 3073–3088  
152 (2004).
- 153 12. LA Miller, CS Peskin, A computational fluid dynamics of clap and fling in the smallest insects. *J. Exp. Biol.* **208**, 195–212  
154 (2005).
- 155 13. LA Miller, CS Peskin, Flexible clap and fling in tiny insect flight. *J. Exp. Biol.* **212**, 3076–3090 (2009).
- 156 14. S Jones, R Laurenza, TL Hedrick, BE Griffith, LA Miller, Lift vs. drag based mechanisms for vertical force production in  
157 the smallest flying insects. *J. theoretical biology* **384**, 105–120 (2015).
- 158 15. C Hamlet, A Santhanakrishnan, LA Miller, A numerical study of the effects of bell pulsation dynamics and oral arms on  
159 the exchange currents generated by the upside-down jellyfish *cassiopea xamachana*. *The J. experimental biology* **214**,  
160 1911–1921 (2011).
- 161 16. G Herschlag, L Miller, Reynolds number limits for jet propulsion: A numerical study of simplified jellyfish. *J. theoretical*  
162 *biology* **285**, 84–95 (2011).
- 163 17. A Hoover, L Miller, A numerical study of the benefits of driving jellyfish bells at their natural frequency. *J. theoretical*  
164 *biology* **374**, 13–25 (2015).
- 165 18. AP Hoover, BE Griffith, LA Miller, Quantifying performance in the medusan mechanospace with an actively swimming  
166 three-dimensional jellyfish model. *J. Fluid Mech.* **813**, 1112–1155 (2017).

- 167 19. AP Hoover, R Cortez, ED Tytell, LJ Fauci, Swimming performance, resonance and shape evolution in heaving flexible  
168 panels. *J. Fluid Mech.* **847**, 386–416 (2018).
- 169 20. AP Hoover, AJ Porras, LA Miller, Pump or coast: the role of resonance and passive energy recapture in medusan  
170 swimming performance. *J. Fluid Mech.* **863**, 1031–1061 (2019).
- 171 21. NA Battista, et al., Vortex dynamics in trabeculated embryonic ventricles. *J. Cardiovasc. Dev. Dis.* **6**, 6 (2019).
- 172 22. JG Miles, NA Battista, Naut your everyday jellyfish model: Exploring how tentacles and oral arms impact locomotion.  
173 *Fluids* **4**, 169 (2019).
- 174 23. B Griffith, X Luo, Hybrid finite difference/finite element immersed boundary method. *Int. journal for numerical methods*  
175 *biomedical engineering* (2017).
- 176 24. IBAMR, IBAMR: An adaptive and distributed-memory parallel implementation of the immersed boundary method  
177 (<https://ibamr.github.io/>) (2014).
- 178 25. SP Colin, et al., Biomimetic and live medusae reveal the mechanistic advantages of a flexible bell margin. *PloS one* **7**,  
179 e48909 (2012).